Part II

Single Pulses

Oh Bonny Pulsar, you shine where you spin
And the more I think on you, the more I think long

adapted from "Bonny Portmore" Irish trad.

Chapter 5

Simultaneous Dual Frequency Observations of Giant Pulses from the Crab Pulsar

5.1 Summary

An analysis of $\simeq$1 ms of signals, approximately 1 hour of 1 pulsar day, from the Crab pulsar.

Simultaneous measurements of giant pulses from the Crab pulsar were taken at two widely spaced frequencies using the detection of a giant pulse at 1.4 GHz at the Very Large Array to trigger the observation of that same pulse at 0.61 GHz at a 25-m telescope in Green Bank, WV.[1] Interstellar dispersion of the signals provided the necessary time to communicate the trigger across the country *via* the Internet. About 70% of the pulses are seen at both 1.4 and 0.61 GHz, implying an emission mechanism bandwidth of *at least* 0.8 GHz at 1 GHz. The arrival times at both frequencies display a jitter of 100 μs within the window defined by the average main pulse profile and are tightly correlated. This tight correlation places limits on both the emission mechanism and on frequency dependent propagation within the magnetosphere. At both frequencies the pulses are characterized by a fast rise time and an exponential decay time. At 0.61 GHz the rise time is not resolved, and the decay is a result of multipath propagation in the ionized gas surrounding the Crab nebula. At 1.4 GHz the giant pulses are resolved into several individual components. The rise and fall times of these components are correlated and vary from component to component and pulse to pulse. This indicates that the broadening does not result from propagation

[1]This is the 85-3 discussed in Chapter 2.

through the interstellar medium. It may be intrinsic to the emission mechanism, or due to propagation within the pulsar magnetosphere, or the product of multiple imaging caused by material in the surrounding nebula. The giant pulse spectral indices fall between -2.2 and -4.9, which may be compared to the average main pulse value for this pulsar of -3.0. The giant pulse contribution to the average increases with frequency, and so the giant pulses must, on average, have flatter spectra than the average main pulse, yet several of the giant pulses have steeper spectra. Several models of giant pulse emission are considered. The giant pulses can be either a temporal or an angular effect, and implications of both models are considered. The broadband nature of the radiation constrains the emission process, which must be coherent.

5.2 Introduction

The Crab pulsar was discovered in 1968 by the detection of its extremely strong individual pulses (Staelin & Reifenstein 1968). Such pulses, which are 100's of times stronger than the average, are not seen in most pulsars. The properties of these giant pulses have been explored for many years (*e.g.*, Heiles, Campbell & Rankin 1970, Staelin & Sutton 1970, Friedman & Boriakoff 1990, Lundgren *et al.* 1995). Giant pulses in the Crab pulsar occur at all radio frequencies, but only at the rotational phase of the main pulse and interpulse components. These two components have counterpart nonthermal emission at high frequencies – from the infrared to gamma ray energies – and may be associated with the outer voltage gaps in the pulsar magnetosphere (Romani & Yadigaroglu 1995). Giant pulses are not seen in the radio precursor or at the phases of the high frequency components recently described by Moffett and Hankins (1996). The radio precursor is identified as being more typical of a radio pulsar and is believed to originate at, and be aligned with, the magnetic pole.

Lundgren *et al.* (1995) found that two separate distributions were required to describe the fluctuations of single pulse energies [2] for the Crab pulsar main pulse and interpulse components at 0.8 GHz. About 2.5% of the pulses lie in the giant pulse distribution with a power law slope extending to high values and a low energy cutoff of 20 times the average of all pulse energies. The distinct distributions suggest different emission mechanisms for the giant and weak pulses and possibly different emission locations within the magnetosphere. However, the lack of an offset in the timing residuals between giant pulses and the average pulse profile (Lundgren 1994; for opposing evidence see Friedman & Boriakoff 1990) suggests that the emission region is the same.

The contribution of the giant pulses to the average energy of all pulses decreases with radio frequency. The probability distribution of the giant pulse energies can be written as

$$P(E_{\rm GP} > E_\circ) = f_\circ \left(\frac{E_\circ}{E_{\rm min}}\right)^{-\alpha},$$

where $f_\circ$ is the frequency of occurrence of the giant pulses, and $E_{\rm min}$ is the minimum

[2] Pulsar emission profiles are generally given in units of *flux* (Jy) even though in the context of rotating neutron stars one actually samples a one dimensional cut of the *specific intensity* pattern (Jy sr^{-1}). The integral of emission over a pulse component in the latter case would be its flux, while in the former and conventional case one quantifies the integrated component emission in units of energy (Jy-s).

energy. Correspondingly the probability density function is

$$p(E_{\rm GP}) = \frac{f_\circ \alpha}{E_{\rm min}} \left(\frac{E_{\rm GP}}{E_{\rm min}} \right)^{-\alpha-1},$$

and the corresponding mean giant pulse energy averaged over all pulses is $\frac{f_\circ \alpha}{(1-\alpha)} E_{\rm min}$. The probability distribution P has a slope $\alpha = 2.3 \pm .15$ at 0.8 GHz (Lundgren *et al.* 1995), and $\alpha = 2.5$ with significant errors at 0.146 GHz (Argyle & Gower 1972). At 1.4 GHz and 0.43 GHz the overall slope is roughly consistent with these, but is not the same for all energies (Friedman & Boriakoff 1990, Moffett 1997). Using the scaling law $\alpha \approx 2.5$ at all radio frequencies below 0.8 GHz, we find that the contribution of giant pulses with energy more than 20 times the average of all pulses, $E_{\rm GP} > 20\, E_{avg}$, is 89% of the average at 0.8 GHz (Lundgren *et al.* 1995), 9% at 0.43 GHz (Friedman & Boriakoff 1990), and only about 1% at 0.146 GHz (Argyle & Gower 1972). The frequency of occurrence of pulses ($f_\circ$) with energy greater than 20 times the average also increases with frequency, from 10^{-4} at 0.146 GHz, to 0.025 at 0.8 GHz. At 1.4 GHz, 80% of the energy comes from the 2% of pulses with greater than 20 times the average energy, using a power law slope of $\alpha = -2$.

There is no evidence of increased flux density in pulses near the giant pulses (Sutton, Staelin, & Price 1971, Lundgren 1994), nor is there any correlation between giant pulses. We note that many pulsars do show strong pulse to pulse correlation in amplitude (the "nulling" phenomenon) and in shape (the "drifting subpulse" phenomenon), indicating a memory process with a duration of many rotational periods. The timescale of giant pulses is, in contrast, less than a single period. In addition, the time separation distribution of giant pulses is consistent with Poisson process (Lundgren 1994).

Despite all these studies, the emission bandwidth of the giant pulses has been poorly determined. Comella *et al.* (1969) found that 50% of giant pulses were seen simultaneously at 0.074 GHz and 0.111 GHz. Goldstein & Meisel (1969) also found that some but not all pulses were correlated between 0.112 GHz and 0.170 GHz. Sutton, Staelin & Price (1971) noted that there was no evidence that the largest pulses at 0.16 GHz and 0.43 GHz were correlated. Heiles & Rankin (1971) observed giant pulses simultaneously at 0.318 GHz and 0.111 GHz, for a bandwidth spread of about 3:1. They found that pulses classified as giant at one frequency were stronger than the average at the other, but not usually classified as giant. Much more recently, Moffett (1997) reported that fully 90% of the giant pulses detected at 4.9 GHz were also detected at 1.4 GHz, implying an emission bandwidth of 3.5 GHz at high radio frequencies. In this paper, we report on giant pulses observed simultaneously at 1.4 GHz and 0.61 GHz to explore the correlation in this intermediate range of frequencies.

Section 5.3 describes the observations, while analysis of the simultaneous pulses lies in Section 5.4.

5.3 Observations

The data shown here were all taken on 1996 May 21 at UT $17^{\rm h}45^{\rm m} - 19^{\rm h}15^{\rm m}$. The 1.435-GHz data were taken at the NRAO Very Large Array (VLA) with all 27 antennas phased to create the equivalent sensitivity of a 130-m antenna, while the 0.61-GHz data were taken using a 25-m telescope at the NRAO Green Bank, WV, site.

The peculiar phases of each antenna at the VLA were determined by observing a standard point-source calibrator. These phases were then applied to the antennas to synthesize a pencil beam pointed at the Crab pulsar, which essentially resolves out the bright Crab Nebula and vastly improves the signal to noise ratio compared to a single-dish antenna. The received voltages from each antenna are summed to form orthogonally circularly polarized 50-MHz bandwidth signals centered at 1.4351 GHz. These are passed through a 1-MHz filter (centered at 1.4356 GHz), then detected and summed with a 100-μs time constant. The detector rms noise power was determined using an rms to DC converter. A detector threshold was set at either 5 or 6 times the running average of this rms noise level. Pulses that exceeded this threshold generated a trigger pulse that was sent to the data recorder, and were then saved to disk and archived to tape using the full 50-MHz bandwidth. In an off-line computer the data were coherently dedispersed using the method developed by Hankins (1971) and described by Hankins and Rickett (1975). Although the ultimate time resolution of the dedispersed data is 10 ns, for the analyses described here the data were smoothed to 0.5 μs after software detection.

The two linearly polarized signals at 0.61 GHz were converted to 90 MHz and 110 MHz, summed, and then sent *via* a single fiber optic link from the 25-m telescope to the Green Bank–Berkeley Pulsar Processor (GBPP) described in Chapter 2, which was at that time located at the 140ft telescope. The GBPP converted the signals to baseband, split these into 32 0.5-MHz channels, and dedispersed the pulsar signal in each channel *via* (de-)convolution in the time domain. The dispersion delay across the 16-MHz bandwidth of the GBPP at 0.61 GHz is about 33 ms, or one pulse period for the dispersion measure of the Crab pulsar ($DM \approx 56.8$ pc cm^{-3}). Full Stokes information was recorded with 982 samples across the pulsar period and an accurate UTC start time for each pulse.

This experiment utilized the difference in pulse arrival time between the two frequencies due to interstellar dispersion to provide the time interval needed to com-

municate the trigger information between the sites. At the VLA, the same trigger pulse that was sent to the data recorder was also sent, as an interrupt, to the SUN workstation used for experiment control and recording. The program that received the interrupt had a socket link open over the Internet to a slave program running on another SUN workstation in Green Bank, and communicated the 1.4356-GHz arrival time of the pulse to Green Bank.

We arranged for the GBPP to begin taking data just before the giant pulse reached the top of the band, in order to obtain data for the same main pulse across the entire band. The dispersion delay between 1.4351 GHz and 0.618 GHz (the top of our 0.61-GHz band) allowed a half second (0.503 s) to arrange this. The SUN workstations at the two sites were synchronized to the local versions of UTC which were derived from accurate atomic clocks using the `xntp` protocol. Both remote sites had 56-kB links to the Internet, with the typical Internet transfer time of 200 ms during our observation. The program running in Green Bank received the trigger message with its VLA time stamp, calculated the transit time of the trigger, and compared that to the dispersion delay difference of 0.503 s. In addition to this delay, the program included other factors such as the difference in pulse arrival due to the separation between observing sites on the Earth and the latency in the GBPP hardware, both of which were of order 1–3 ms. If sufficient time remained, it waited until the appropriate time and issued a trigger to the GBPP via the SUN parallel port to take data for the next pulse period. Due to the slow rate of data transfer from the GBPP, it could only accept such a command approximately every 12 seconds. Some VLA-initiated triggers were therefore missed by the GBPP.

The Stokes parameters for the high-time resolution data from the VLA were formed from the dedispersed voltages. To obtain the necessary 90° phase shift a FIR approximation to the Hilbert Transform was applied to the right circular polarization signal before forming the Stokes parameters. No instrumental polarization corrections were made other than bandpass leveling and gain matching; concurrent calibration (Moffett 1997) has shown that the polarization cross-coupling is less than 10% for the VLA phase array. The polarization error then is comparable with the radiometer uncertainty imposed by the limited number of degrees of freedom in the data ($(\Delta\nu\,\Delta\tau)^{-1/2} = 0.14$) in Figure 5.1).

The single pulse polarization profiles at 0.61 GHz were calibrated using factors derived from pulsed noise observations. The telescope introduces a relative phase between the two linear polarizations which couples the Stokes parameters U and V. This phase was determined and removed using nearby observations of the Vela pulsar, and comparison to a template polarization profile, as described in Section 2.5.5.2. No attempt has been made to remove coupling between the two polarizations. The error

in polarization due to improper calibration is estimated at 10%. For each pulse, the relative dispersion between the 32 channels was removed, and the resultant data were summed over channels, after first removing the effects of the pulsar's rotation measure ($RM = -42.3$ rad m^{-2}) across the band. The ionosphere could cause an additional rotation of 1 to 10 degrees across the total band, and has not been removed. Incomplete removal of rotation measure causes depolarization of the resulting pulse profiles.

5.4 Analysis

5.4.1 Wide Bandwidth Correlation

Of the 85 triggers initiated at the VLA a total of 77 trigger events reached Green Bank within the required time, and were accepted by the GBPP. The `xntp` protocol requires 24 hours to stabilize to the accuracy required by our experiment. The minimum time stabilization period was not available for the SUN at the VLA. Consequently the VLA clock used to identify the time at which the trigger was sent drifted by a small amount. For this reason, and others, we are currently only certain that we observed the correct period with the GBPP for 42 pulses.

The arrival times and pulse energy amplitudes were determined at both frequencies for each of these pulses. The 0.61-GHz arrival times were determined by cross-correlation with a model template, which consisted of a single-sided exponential with a decay time scale of 3 time bins, about 100 μs. The pulse amplitude was defined as the integral of the on-pulse energy in units of Jy-s. At 0.61 GHz, this was determined by removing an off-pulse average, then summing the flux in the time bins from 1 before the peak to 6 after the peak (accounting for fractional bins as determined in the cross-correlation). The 1.4-GHz pulse arrival times were obtained by computing the location of the centroid of the pulses; the amplitude was computed as the total energy received for each pulse by integrating its flux, after first removing the off-pulse baseline level.

We definitely detected 29 of the 42 correctly timed pulses at both radio frequencies. This corresponds to a 0.61-GHz pulse energy threshold of about 4.5 times the typical measurement uncertainty, or 0.075 Jy-s using 0.14 K Jy^{-1} for the 25-m telescope. This gain factor was determined using on and off measurements of the Crab nebula, and has an estimated uncertainty of 50%. We conclude that about 70% of the pulses are detected at both frequencies. The remaining pulses may be giant pulses that are too weak to be seen with the 25-m telescope at Green Bank, or may be normal pulses too weak to be classified as giant.

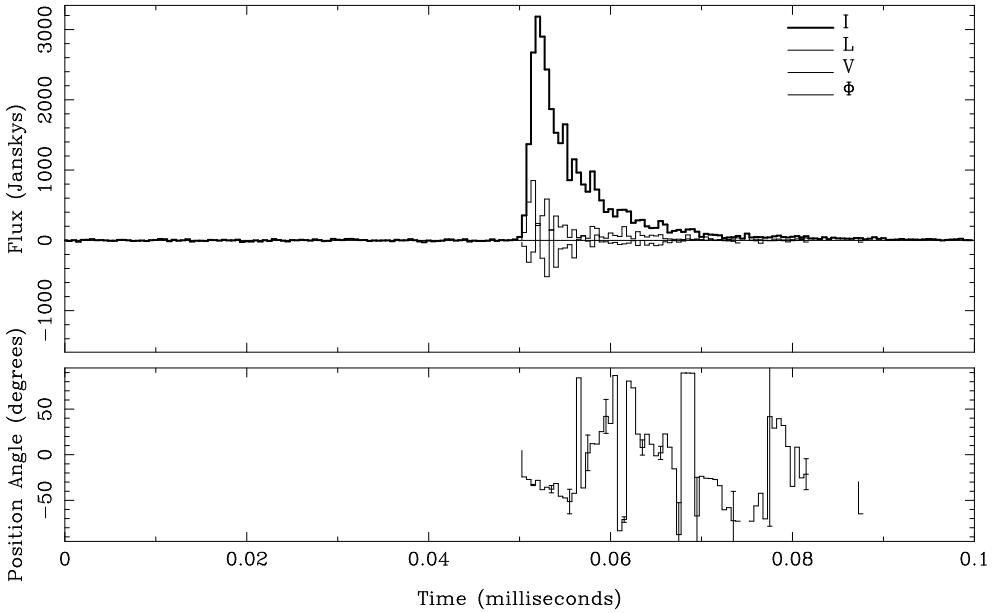

Fig. 5.1.— This figure displays the data for a single giant pulse at 1.4 GHz, taken at the VLA on 1996 May 21, with a temporal resolution of 0.5 μs. The top panel displays the total intensity I, along with linear and circular polarizations L and V. The vertical scale indicates that this pulse reached a peak flux of 3000 Janskys. The lower panel indicates the position angle of the linear polarization across the pulse.

The data for a single giant pulse at 1.4 GHz and 0.61 GHz are displayed in Figures 5.1 and 5.2, respectively. This pulse is strongly polarized at both frequencies, although fully two thirds of the giant pulses at the lower frequency are consistent with zero polarization. The 0.61-GHz data has a low number of degrees of freedom, and so the polarization estimation uncertainty is about 5%. At 1.4 GHz, the typical polarization is about 8% although at least one pulse is 50% polarized. The position angle of the linear polarization generally varies significantly across the pulse, as is seen in Figure 5.1.

The arrival times for the 29 giant pulses detected at the two frequencies were separately compared to a single model for this pulsar using the TEMPO program developed for pulsar timing (Taylor & Weisberg 1989). For each radio frequency, the arrival times are well-represented by the model, leaving timing residuals of order $\pm 100\mu$s. The residuals are comparable to the pulse width of the average profile during periods of low scattering, which is 275 $\pm 50\mu$s (FWHM) at 0.61 GHz, and 257 $\pm 50\mu$s at 1.395 GHz (*cf.* section 5.4.4).

The residuals for 1.4 and 0.61 GHz are plotted against one another in the top panel of Figure 5.3, which shows that they are highly correlated. The solid line has a slope of 1 and goes through the origin. In order for the points to fall along this

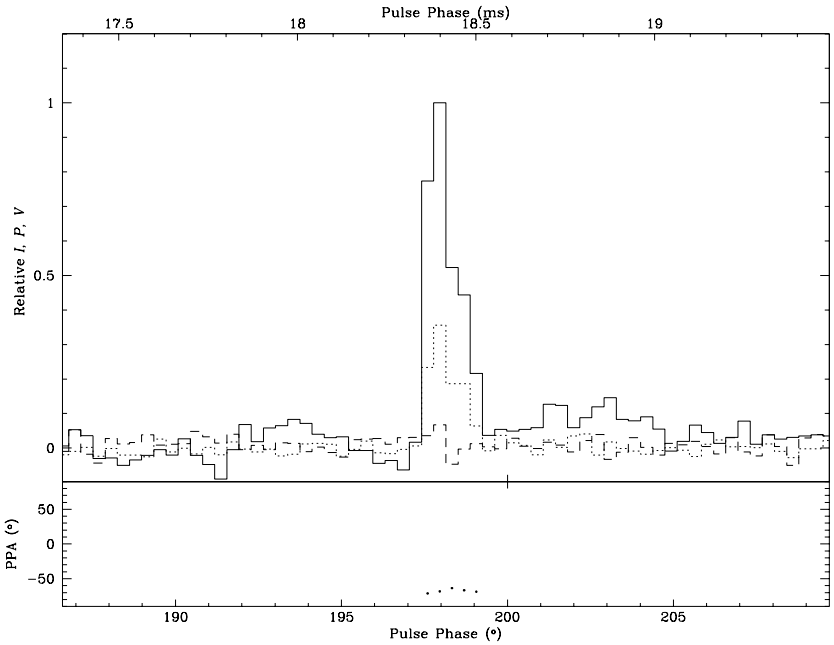

Fig. 5.2.— Figure 5.2 displays data for the same single pulse at 0.61 GHz, taken with the GBPP. The temporal resolution is approximately $34\mu s$. The top panel displays the total intensity I, along with linear and circular polarizations L and V. The peak flux for this pulse was $\approx$ 7000 Jy. The negative and positive features on either side of the main peak are artifacts due to the non-linear response of the GBPP. The lower panel indicates the position angle of the linear polarization across the pulse. Here only points with $L > 3$ times the off pulse rms noise are shown.

line, the 1.049 ms digital latency of the GBPP and the 235.42 μs latency of the VLA samplers and delay lines were removed, and a further fit for dispersion measure was done in TEMPO. The derived DM is 56.830 pc cm^{-3} although systematic errors may remain in the arrival times from the two sites. The bottom panel displays the same 1.4-GHz residuals with the solid line removed.

Eilek (1996) has shown that the dispersion law in the polar cap is different from that in the interstellar medium, proportional to ν^{-1}, as opposed to ν^{-2} for the cold interstellar medium (ISM). No systematic trends remain in the data in the lower panel of Figure 5.3, indicating that systematic variations with pulse phase from the differential effects of propagation through the magnetosphere are less than $\pm 15\mu$s between our two bands, corresponding to an angle of 0.164 degrees of pulsar rotation phase, or a range of 4.5 km in altitude. It would have been possible to have correlated emission from subpulses at different pulse longitudes at each frequency. In this case, the radiation at the two frequencies need not have come from the same radiating unit of charges. The observed rms jitter in arrival time at either frequency is $\approx$ 100 μs, so the fact that the difference between the residuals has such a small dispersion indicates that the emission must be from the same radiating unit at both frequencies.

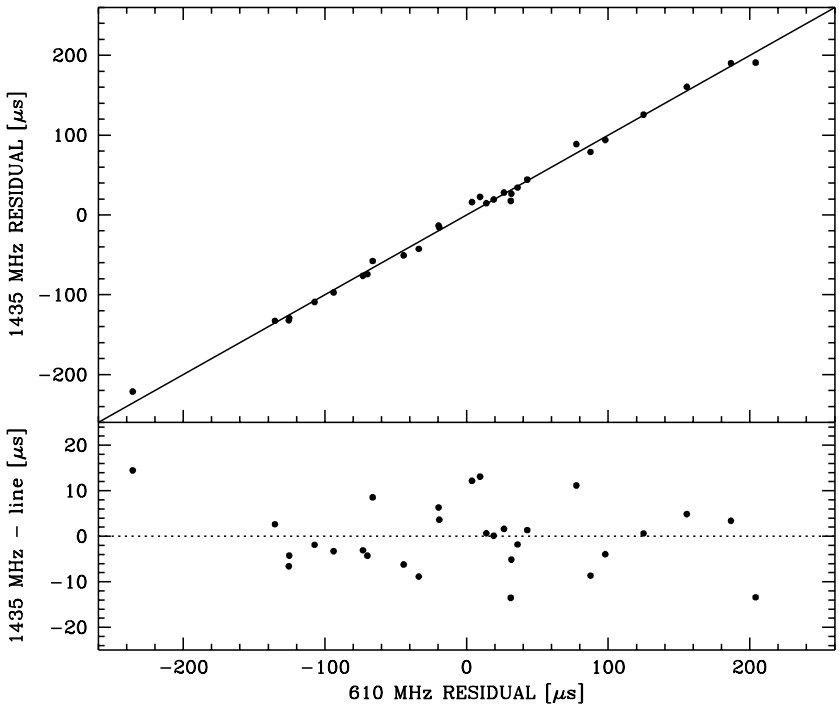

Fig. 5.3.— The top panel of Figure 5.3 displays the 1.4-GHz timing residuals against the 0.61-GHz timing residuals. The solid line passes through the origin with slope 1. The bottom panel displays the same data with this line removed.

This means that 70% of the giant pulses must have a bandwidth of *at least* 0.8 GHz at 1 GHz. The emission is clearly wide band for these cases, as expected for models wherein the fundamental radiating unit has a scale of about 30 cm and emits a pulse of nanosecond width.

5.4.2 Profile Shape

The giant pulses at 0.61 GHz all have profiles displaying a fast rise, followed by an exponential decay, similar to the profile shown in Figure 5.2. The fast rise indicates that the intrinsic time scale of the pulse is unresolved, $\lesssim 10\mu$s. The exponential decay time scale is $90-100\mu s$. At the time of these observations, the Crab was undergoing a period of unusually large scattering, as evidenced by monitoring of pulse broadening at 0.327 GHz using the 25-m telescope (Backer & Wong 1996). The scattering time scale at 0.327 GHz from these monitoring observations was $\tau_{\rm ISS}(0.327\ {\rm GHz}) = 1.3\pm0.2$ ms, which can be compared to 0.28 ms at an earlier epoch. The enhanced value at the time of our observations is presumably the result of a turbulent ionized filament in the periphery of the Crab nebula passing through the line of sight owing to motions of both the filament and the pulsar. The 0.61-GHz exponential decay time scale for these observations is therefore consistent with multipath propagation in the intervening perturbed plasma.

The giant pulses at 1.4 GHz have a wide variety of shapes. Figures 5.4 and 5.5 display two further single pulse profiles. The first pulse is extremely narrow, and is dominated by a single component, while the second has several components contributing to the emission. The darker solid line is a model fit to the data, where the model $S(t)$ consists of up to six components, and is of the form $S(t) = \sum_{i=1}^{n} a_{1_i}(t - a_{2_i})e^{-(t-a_{2_i})/a_{3_i}}, \quad n \leq 6$. These components rise to their peak in a time a_3, fall by e^{-1} in a further $2.15a_3$, and have a pulse energy amplitude of $a_1 a_3^2$. The majority of giant pulse components are well represented by this model, with widths a_3 ranging from 1.2 μs to 10 μs. At 1.4 GHz, the narrow component of the giant pulse shown in Figure 5.4 has a rise time of 1.2 μs, and a decay time scale of 2.5 μs. The second fitted component is clearly necessary to account for the emission on the trailing edge of the pulse, which does not follow an exponential tail. Thus the interstellar scattering time scale must be $\tau_{\rm ISS}(1.4\ {\rm GHz}) \lesssim 2.5\mu$s.

If the scattering along the line of sight obeys a Kolmogorov spectrum, then $\tau_{\rm ISS}(\nu) \propto \nu^{-4.4}$ and, based on the 0.327-GHz data, we expect $\tau_{\rm ISS}(1.4\ {\rm GHz}) = 1.9 \pm 0.3\mu$s, which is comparable to the observed minimum decay value of 2.5 μs. If the spectrum of the nebular material is not Kolmogorov, but follows a law more like $\tau_{\rm ISS}(\nu) \propto \nu^{-4}$, then the expected $\tau_{\rm ISS}(1.4\ {\rm GHz}) \approx 3.5\mu$s, which is somewhat larger than the observed minimum decay time. We conclude that the *minimum* component width at 1.4 GHz *is* a result of ISS. A future experiment during an interval of reduced scattering is planned to determine the intrinsic pulse width.

Many giant pulse components possess much longer time scales than 2 μs, although they are still well characterized by the functional form of the xe^{-x} fit. For example,

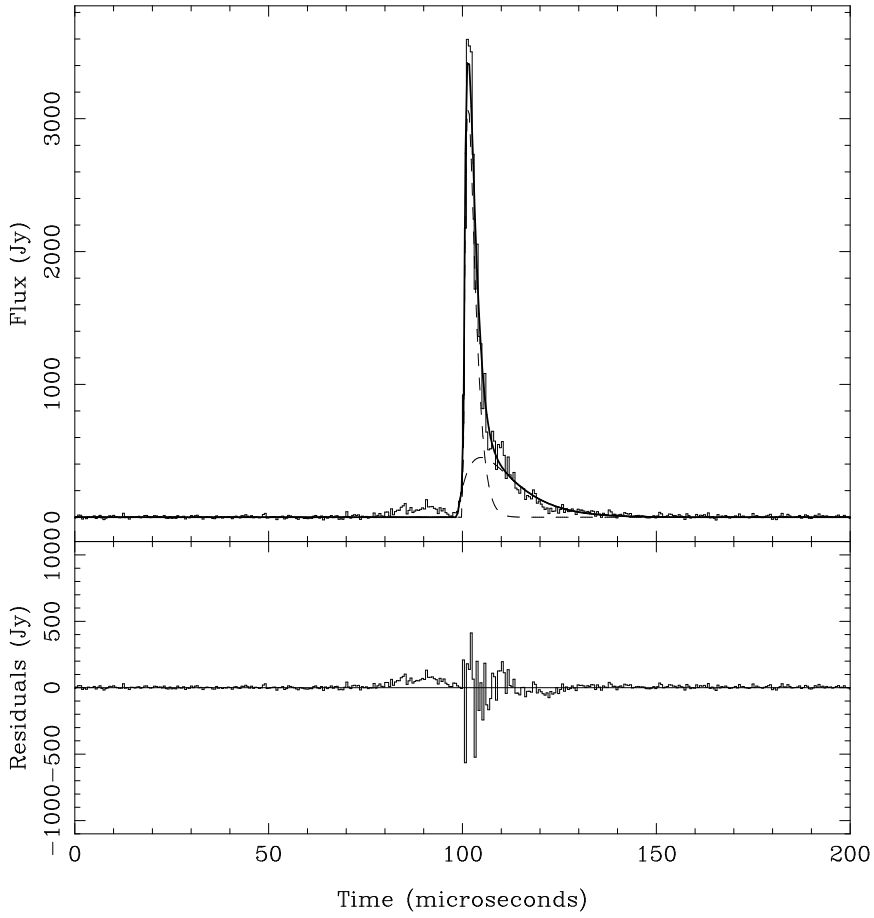

Fig. 5.4.— Figure 5.4 displays an example of a 1.4-GHz single pulse profile. The intensity data are modelled by the dark solid line, which is created using the fitted components represented by the dashed lines. These components are characterized by a fast, nearly linear rise, followed by an exponential decay. The narrow component of the giant pulse shown here has a characteristic time scale of 1.2 μs.

the final component of the pulse displayed in Figure 5.5 has a decay time scale of 12.3 μs. Furthermore, pulses such as this one clearly display several xe^{-x} components superposed with different decay times. Both pulse to pulse variations and component to component variations are not consistent with scattering in a distant screen. We conclude that these variations are intrinsic to the immediate vicinity of the pulsar.

These fitted components of the form te^{-t/a_3} are bunched within the window defined by the average main pulse. The distribution of their separations is not consistent with a random scattering of components within the average pulse window. The energies $a_1 a_3^2$ are independent of pulse width a_3, have an average of 6.3×10^{-3} Jy-s, and are scattered over two orders of magnitude. This means that the peak flux scales with

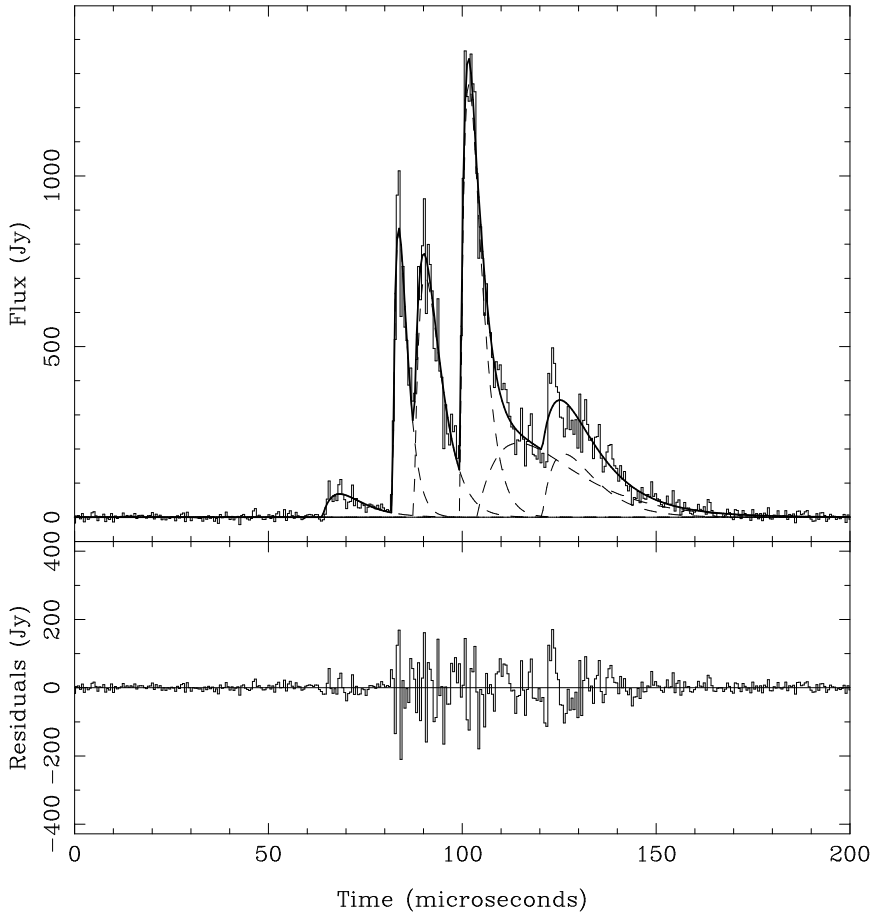

Fig. 5.5.— Figure 5.5 displays an example of a complex 1.4-GHz single pulse profile. The intensity data are modelled by the dark solid line, which is created using the fitted components represented by the dashed lines. These components are characterized by a fast, nearly linear rise, followed by an exponential decay. The final component of the giant pulse shown here has a characteristic time scale of 5.7 μs.

a_3^{-1}, and the energy scales with a_3^{-2}. It is possible that the bunching of components is due to multiple imaging of the pulse by refraction in the nebula surrounding the pulsar (Cordes, Hankins & Moffett 1998, in prep.). These may be associated with bright, dense optical filaments. If this cannot explain the observed shapes, then either the emission of a component is intrinsically asymmetric with linear growth, saturation and decay phases in time, or intrinsically narrow pulses of emission are variably spread as they exit the pulsar magnetosphere. These possibilities are further discussed in Section 5.4.5.

5.4.3 Energies and Spectral Indices

Lundgren *et al.* (1995) concluded (*cf.* section 5.2) that if the emission is narrow band, the rate of giant pulses must increase with frequency, while if the emission is broad band, then the giant pulses must have flatter spectra than the weak pulses. At least 70% of the pulses are broadband, so we expect their spectral indices to be, on average, flatter than the average main pulse spectral index.

Figure 5.6 displays 1.4-GHz and 0.61-GHz pulse energy amplitudes against one another, for the 29 pulses detected at 0.61 GHz. The 1.4-GHz amplitudes of the 13 pulses which were certainly not detected at 0.61 GHz are also shown. The vertical dashed line indicates our estimate of the threshold used at the VLA, and the horizontal dashed line represents the amplitude cutoff corresponding to the 0.61-GHz detection of pulses at Green Bank. Solid lines corresponding to spectral indices -2.2 and -4.9 are also shown, where spectral index q is defined by $A_{\rm GB}/A_{\rm VLA} = (0.61/1.4)^q$. The pulse amplitude of the average main pulse, shown as a horizontal dotted line in Figure 5.6, is 5.4×10^{-3} Jy-s at 0.61 GHz. The largest 0.61-GHz giant pulse therefore has a pulse amplitude of about 150 times the amplitude of the average pulse. The giant pulses are narrower than the average pulse, and so are even stronger relative to the average pulse within this window.

The spectral indices of the giant pulses detected at both frequencies fall between -2.2 and -4.9, with an average of -3.4. Moffett (1997) found that between 1.4 and 4.9 GHz, giant pulse spectral indices ranged from 0 to -4, with an average of about -2. At least 2 of the pulses in our sample which were undetected at 0.61 GHz *must* have flatter spectral indices if they are giant but too weak to be seen. The overall spectral index for the Crab pulsar is -3.1, while the spectral index for the average main pulse is -3.0, and is shown as a dotted line in Figure 5.6 (Moffett 1997). Despite the expectation that the average giant pulse should have a flatter spectrum than the average, we see many giant pulses steeper than the main pulse index of -3.0. The average spectral index of the giant pulses is -3.4, but this estimate is biased by the fact that the undetected giant pulses could contribute flatter spectral indices, and by possible systematic errors in flux calibration, which could change the average spectral index by up to 0.4. Alternatively, these pulses may simply not be giant at the lower frequency, which would indicate that the giant pulse emission process is not always broadband. The 30% which are missing are insufficient to explain the strong variation with frequency in the energy contribution of the giant pulses, if the typical giant pulse spectral index matches that of the average main pulse. The measured scatter in spectral indices of the giant pulses indicates that this is not the case, and the distributions will transform in a more complicated fashion.

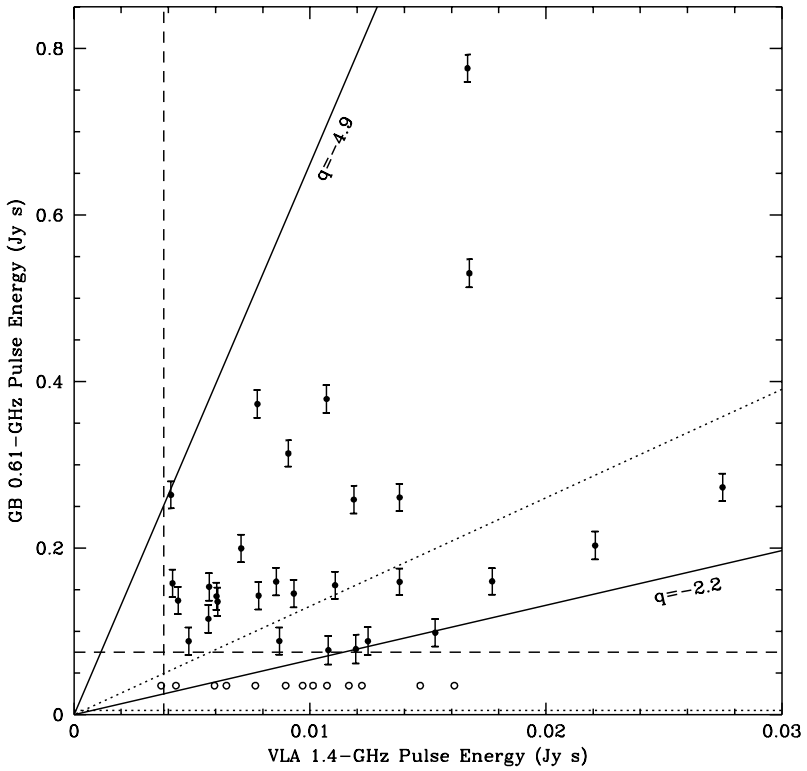

Fig. 5.6.— This figure displays the pulse energy amplitudes in Jy-s at 0.61 GHz and 1.4 GHz. The solid circles denote the 29 pulses which were detected at both frequencies. Error bars reflect the measurement uncertainty, which is negligible for the 1.4-GHz data. Uncertainty in the K Jy^{-1} calibration used at 0.61 GHz introduces an additional systematic uncertainty of 50%. The open circles represent those pulses seen at 1.4 GHz which were certainly not detected at 0.61 GHz. The horizontal dashed line represents the cutoff of 0.075 Jy-s, below which we could not detect pulses at 0.61 GHz. The vertical dashed line indicates our estimate of the VLA threshold corresponding to 6 times the rms noise. The one pulse with a 1.4-GHz energy less than this occurred while our threshold was 5 times the rms noise. The solid lines represent spectral indices $q = -2.2$ and $q = -4.9$. The dotted lines indicate the average main pulse energy and spectral index.

The individual giant pulse spectral indices display a relatively large scatter. Similarly, Heiles & Rankin (1971) found that their measured spectral indices at low radio frequencies ranged from nearly 0 to less than -3.0. There are several possible explanations. The spectral index variations could be due to the stochastic uncertainty in the determination of the amplitudes, introduced by the low number of degrees of freedom. We estimate this uncertainty to be of order 10% at 1.4 GHz, for an intrinsic pulse width of 1 μs. At 0.61 GHz, this is estimated to be less than the measurement uncertainty for the pulse energy. These are not large enough to explain the scatter in the spectral indices. The scatter could also be intrinsic to the radiation emission process. The signal could consist of a randomly occurring series of nanosecond im-

pulses whose Fourier transform in power is irregular. This would cause scatter in the observed spectral indices. But with the radiation extending over a few to 10 μs, there are many nanosecond pulses which might be expected to smooth out this distribution. Alternatively, one might expect the spectral index to vary due to properties of the emission beam.

5.4.4 Models of the Emission Beam

There are several possible models for giant pulse emission. In the temporal model, the enhanced emission is turned on only when we see a giant pulse, but covers the same beam as the average pulse, and has the same amplitude shape. Following Lundgren (1994), we also consider a model in which the enhanced emission is due entirely to a steady pencil beam with a random angular wobble. We see a giant pulse when the beam enters the line of sight. In both models, the average beam may be circular, as in polar cap models, or fan-shaped, as is likely if the emission comes from the outer gaps.

In the temporal model, if the width of the average beam varies with frequency, then the spectral index of the average pulse varies with pulse longitude. Using the data of Moffett & Hankins (1996) at 4.8 GHz, along with GBPP data from the 25-m telescope at 0.61 GHz, and from the 140ft telescope at 1.4 GHz, we performed Gaussian fits to determine the average component widths. We find that the main pulse width (FWHM) is $3.0 \pm .5$ degrees at 0.61 GHz, $2.8 \pm .5$ degrees at 1.4 GHz, and $3.5 \pm .5$ degrees at 4.8 GHz, implying that it does not vary significantly with frequency. Then the spectral index of the average pulse is not expected to vary across the pulse. A plot of our measured spectral indices *vs.* arrival time residuals at 0.61 GHz in fact shows no systematic variations. If the average beam varied with frequency, this would detract from the temporal model. This lack of variation cannot rule out the temporal model in this case because the width of the average beam is independent of frequency.

In the model with steady emission from a wobbling pencil beam, the width of the giant pulses $w_{\rm gp}$ corresponds to the size of the beam. If the intrinsic width of the giant pulses varies with frequency, then the observed spectral index will depend on how directly we are viewing the pencil beam. This model could explain the scatter in our spectral indices. Current measurements of giant pulse widths do show a small variation in width with frequency, which does not follow the Kolmogorov law, but the lower frequency data are contaminated by the effects of interstellar dispersion (Moffett 1997). The wobbling beam may also provide an explanation for the scatter in the energies of our fitted components. If the beam has a Gaussian intensity distribution,

then the observed energy again depends on the line of sight, with the most central ones producing the largest energy.

In this angular model, the pencil beam of emission may wobble in either the l direction (along the trajectory of the line of sight, a line of constant latitude), or the ϕ direction (perpendicular to the trajectory of the line of sight, a change in latitude). The width of the giant pulses corresponds to the size of the beam in this model, while the jitter in arrival times $\sigma_{\rm toa}$ corresponds to the wobbling of the beam along l. For giant pulses which occur a fraction f of the time, the wobble in ϕ is then $w_{\rm gp}/(Pf)$ where P is the pulse period (following Lundgren *et al.* 1995). Lundgren was able to separate the giant pulse and normal pulse distributions at 0.8 GHz, and found that 1 of 40 pulses is giant. At 1.4 GHz we see that the intrinsic width of the giant pulses is $w_{\rm gp} \approx \pm 1 - 10\mu$s. Since the giant pulses form a separate distribution, then if they are all broadband, they will all appear at both radio frequencies. Then at 1.4 GHz, 1 of 40 pulses should be giant. In fact, Moffett (1997) finds that one of 50 pulses has an energy greater than 20 times the average. We find $\sigma_{\rm toa} \approx 100\mu$s, so the 0.01 to 0.1-degree beam then wobbles 1.1 degrees in l and 0.5 to 5 degrees in ϕ. This is consistent with a pencil beam wobbling within a roughly circular average beam. If the average beam is a fan beam, it will be elongated in the ϕ direction. Given that the giant pulses dominate the emission at 1.4 GHz, they must stochastically fill the fan beam. This is impossible in this model unless the giant pulse beam is also elongated parallel to the fan beam, or multiple round pencil beams fill the average fan beam.

5.4.5 The Emission Mechanism

Radio emission from pulsars must come from a coherent emission process (Cordes 1981). The exact process is very uncertain, as is the location of the emission. It is not necessary for the giant pulse emission to originate at the same place or in the same way as the weak pulse emission. The broadband nature of the giant pulse emission provides the main constraint on its origin. According to Melrose (1996), broadband emission is traditionally associated with models in which the emission occurs at a pair production front in the polar cap, or *via* Schott radiation from a corotating charge and current distribution outside the light cylinder (*e.g.*, da Costa & Kahn 1985; Ardavan 1992, 1994). The emission process itself could rely on plasma instabilities (Cheng & Ruderman 1977, Asséo 1993, Machabeli & Usov 1979, Kazbegi *et al.* 1991). Alternatively, other maser processes such as linear acceleration emission (Melrose 1978, Rowe 1995) or maser curvature emission (Luo & Melrose 1992, 1995) could produce the radiation. In any case, if the giant pulses are a temporal effect, this variability in radio emission could be due to variations in the number of coherently

emitting regions (incoherently summed), or an increase in the coherence within a single emission region.

Given the characteristic shape of the giant pulse components at 1.4 GHz, any model producing giant pulse radiation must be characterized by an approximately linear rise, followed by an exponential decay. This intrinsically asymmetric shape is not expected for a simple pencil beam with an angular wobble. In either model, this shape can be explained by propagation in the magnetosphere (Eilek, Hankins & Moffett 1998), or in the medium immediately surrounding the pulsar. The effects of aberration are too small to produce the broadening and asymmetry seen in these pulses, if one confines the range of emission altitudes to 4.5 km, according to the difference between the residuals at the two frequencies. In the temporal model, this shape is consistent with any emission process which turns on with a rapid nearly linear rise, then saturates and decays. In this case one would expect the peak energy to be independent of width, whereas we have seen that it is the total pulse energy which is independent of width.

We assume that the shape is intrinsic to the emission mechanism and consider a temporal model in which a bunch of charges radiates so as to produce a single pulse component. For coherent curvature radiation, the power lost by the N excess charged particles in the bunch will be

$$P_{curv} = N^2 \left(\frac{2e^2\gamma^4 c}{3\rho_c^2} \right),$$

where e is the charge on an electron, γ is the relativistic factor $(1 - v^2/c^2)^{-1/2}$, and ρ_c is the radius of curvature of the magnetic field. We observe 6.3×10^{-3} Jy s in a 50-MHz band, so P_{curv} must equal the measured luminosity, which is therefore greater than 4.3×10^{22} erg s^{-1}, assuming a distance of 2 kpc, and a circular beam 100 μs $= 1^\circ$ wide. Then the number of particles in the bunch must be at least

$$N = 3.07 \times 10^{19} \left(\frac{\gamma}{100} \right)^{-2} \left(\frac{\rho_c}{10^8 \mathrm{cm}} \right).$$

These particles must fit within a cube with volume $\leq \lambda_{em}^3$, so the number density of excess charges must be $\delta n_e = N/\lambda_{em}^3 = N/(\gamma\lambda_{obs})^3 = 3.3 \times 10^9$ cm^{-3} for the parameters used above, and a wavelength of 21 cm. This density can be further reduced if several bunches are radiating in a periodic structure.

If the model is truly temporal, then the angular size of the beam does not affect the pulse width. The radiation will be beamed into a beam width $\theta \sim \gamma^{-1}$. Requiring that the beam be wider than 50μs, so it is wider than any given pulse component, then implies that $\gamma \lesssim 100$. Since complex pulses such as the one shown in Figure

5.5 have many overlapping pulse components, we must have several bunches whose radiation adds incoherently to produce the observed profiles. The radiation from one bunch must not affect the charges in another bunch. For a temporal separation Δt between components, this restriction is satisfied for bunches with an angular separation of $\Delta\theta = 2\pi\Delta t/P$, which corresponds to a horizontal separation of $\Delta s = r\Delta\theta$. Given a component separation of 10 μs, we find $\Delta s = 1.9$ km for an emission height of 10^8 cm, a substantial fraction of the distance to the light cylinder. The same temporal separation could be achieved with two bunches at altitudes differing by $c\Delta t/(1+\sin i) \sim 3$ km, but the radiation from the lower bunch would affect the upper one. If the two bunches are separated both horizontally and vertically, the observed time separation must include the angular, time-of-flight, and aberration effects, and the bunch at the higher altitude must be sufficiently separated horizontally to be out of the γ^{-1} beam of the lower bunch. For the parameters above, and $\gamma = 100$, this means that $\Delta s \geq 7.5$ m, and $\Delta r \leq (c\Delta t + \Delta s)/(1 + \sin i) \sim 1.5$ km for $\Delta s = 7.5$ m.

As suggested in Section 5.4.2, the multiple components can be explained by a single emitted pulse that is multiply imaged by finite-width plasma structures near the pulsar (Cordes, Hankins & Moffett 1998). This model can also explain the high frequency deviation of observed giant pulse widths from the $\upsilon^{-4.4}$ dependence that is otherwise expected (Moffett 1997). One prediction of this model is that late-arriving pulses should be broader. This test has not yet been performed, but should be possible with 1.4-GHz data taken at the VLA. Of additional interest is whether the range of 1.4-GHz broadening times remains constant, or is larger during this epoch of unusually large scattering. If it is the same even when the scattering at low frequencies is smaller, then the finite-width structures causing the multiple images are not the same as the material causing the variations in pulse broadening at low frequencies.

5.5 Conclusion

Simultaneous dual frequency observations of giant pulses from the Crab pulsar reveal that the emission is broadband, since 70% of the pulses are observed at both frequencies. The tight correlation in arrival times implies that the same radiating unit is operating at both frequencies. The pulses are characterized by a fast rise and exponential decay, which cannot be entirely due to interstellar scattering at the higher frequency. The giant pulses display a scatter in spectral index, which is not due to measurement uncertainty. Pulsar emission models are restricted to those which can explain the broadband nature of the giant pulse radiation.